






Cite this: *Nanoscale*, 2023, **15**, 17076

# A bi-functional three-terminal memristor applicable as an artificial synapse and neuron†

Lingli Liu,  Putu Andhita Dananjaya, Calvin Ching Ian Ang, Eng Kang Koh,   
Gerard Joseph Lim, Han Yin Poh, Mun Yin Chee, Calvin Xiu Xian Lee  and  
Wen Siang Lew \*

Due to their significant resemblance to the biological brain, spiking neural networks (SNNs) show promise in handling spatiotemporal information with high time and energy efficiency. Two-terminal memristors have the capability to achieve both synaptic and neuronal functions; however, such memristors face asynchronous programming/reading operation issues. Here, a three-terminal memristor (3TM) based on oxygen ion migration is developed to function as both a synapse and a neuron. We demonstrate short-term plasticity such as pair-pulse facilitation and high-pass dynamic filtering in our devices. Additionally, a 'learning–forgetting–relearning' behavior is successfully mimicked, with lower power required for the relearning process than the first learning. Furthermore, by leveraging the short-term dynamics, the leaky-integrate-and-fire neuronal model is emulated by the 3TM without adopting an external capacitor to obtain the leakage property. The proposed bi-functional 3TM offers more process compatibility for integrating synaptic and neuronal components in the hardware implementation of an SNN.

Received 12th June 2023,  
Accepted 4th October 2023

DOI: 10.1039/d3nr02780e

rsc.li/nanoscale

## Introduction

As the demand for the Internet of Things (IoT) and artificial intelligence (AI) continues to grow, the increasing power consumption resulting from the physical separation of memory and processors in traditional von Neumann architectures has become a compelling concern.<sup>1</sup> Motivated by the biological brain's ability to perform diverse functionalities with a massively parallel architecture consisting of neurons and synapses, the concept of neuromorphic computing was proposed.<sup>2</sup> A biological neuron works to receive the input from the presynaptic neuron through dendrites, processes the inputs in the soma, and transmits the processed signal downstream along axons to the postsynaptic neuron if the integrated input reaches a threshold. Synapses play a vital role by acting as junctures between dendrites and axons, fine-tuning the communication network within and between neurons. Analogous to the human brain, a neuromorphic computing system consists of artificial neurons and synapses.<sup>3</sup> So far, various electronic devices have been proposed to demonstrate the synaptic and neuronal functions for efficient hardware implementation of artificial neural networks (ANNs).<sup>4,5</sup> A spiking neural network (SNN) aims at mimicking the biological neural networks more

closely by incorporating the concept of time into the operating model. It encodes spatiotemporal information within the neurons, which transmit information only when the membrane potential reaches a specific threshold.<sup>6–8</sup> Thus, an SNN offers a promising alternative to an ANN with higher energy efficiency.

The hardware integration of both artificial synapses and neurons into an SNN still faces enormous challenges in terms of process incompatibility.<sup>9</sup> A developed device that has both synaptic and neuronal functions would be an ideal mitigation. One approach is to leverage complementary metal–oxide–semiconductor (CMOS) transistor technologies, with the realization of neuronal functions *via* external or parasitic capacitors.<sup>10–12</sup> Han *et al.* presented a highly scalable transistor with the capability of acting as both a neuronal and a synaptic device.<sup>10</sup> Another approach is using two-terminal memristor-based artificial devices. Despite having a highly scalable footprint, these devices are unable to perform synchronous read/write operations due to the shared read/write path.<sup>7,9,13–15</sup> In addition, due to the underlying physics of the device switching mechanisms, the devices tend to have large spatial and temporal variations of conductance modulation under an external electric field.<sup>16–18</sup> To overcome this challenge, a more promising candidate appears to be the three-terminal memristor (3TM), offering decoupled writing and reading paths.<sup>19,20</sup> Zhang *et al.* reported a 2D material-based bi-functional device, demonstrating high face recognition accuracy in a hardware system.<sup>19</sup> Nevertheless, the incorporation of a polymer into

School of Physical and Mathematical Sciences, Nanyang Technological University, 637371, Singapore. E-mail: WenSiang@ntu.edu.sg

† Electronic supplementary information (ESI) available. See DOI: <https://doi.org/10.1039/d3nr02780e>

the device may pose an integration compatibility issue with CMOS circuitry. Therefore, there are clear advantages to designing a CMOS-compatible 3TM device with synaptic and neuronal functions. In this work, a 3TM device governed by gate-controlled oxygen ion migration (O-3TM) to achieve synaptic and neuronal bi-functionality is developed. Oxygen ions ( $O^{2-}$ ) can act as mobile ions in ionic synaptic transistors, which are more sustainable than their proton- or lithium-ion-based counterparts.<sup>21–25</sup> By applying a positive voltage to the gate of O-3TM, the induced electric field governs the  $O^{2-}$  migration from a channel to the electrolyte, or *vice versa*, to realize the synaptic weight updating. The concentration gradient of  $O^{2-}$  at the channel/electrolyte interface allows self-migration of  $O^{2-}$ , enabling O-3TM to successfully mimic fundamental synaptic behaviours, including excitatory postsynaptic current (EPSC), paired-pulse facilitation (PPF), and learning-forgetting-relearning abilities. Additionally, leaky-integrate-and-fire (LIF) neuronal functions are also demonstrated in this O-3TM.

## Results and discussion

### Device *I*-*V* characteristics

The O-3TM utilizes  $WO_x$  as the channel and  $HfO_2$  as the electrolyte. The optical image and schematic diagram of the device are depicted in Fig. 1a and b, respectively. The obtained X-ray photoelectron spectroscopy (XPS) spectra of the  $WO_x$  film are shown in Fig. S1,<sup>†</sup> in which the mixed valences of tungsten as well as the O-W bonds with a certain amount of O vacancies can be detected. Such a non-stoichiometric  $WO_x$  has been used as a channel material due to its abundant oxygen storage sites.<sup>21,23,26</sup> Fig. 1c shows the transfer characteristics of the O-3TM, obtained by sweeping the gate voltage ( $V_{GS}$ ) from 0 V to 3 V, followed by 3 V to -3 V, and then -3 V back to 0 V. The inset of Fig. 1c gives the transfer curve in a log-linear scale. The interval between each increment is kept at 4 mV, while maintaining the drain voltage ( $V_{DS}$ ) at a constant value of 0.2 V. Referring to the anticlockwise arrows shown in the plot, the increase in current appears after the positive  $V_{GS}$  reaches a

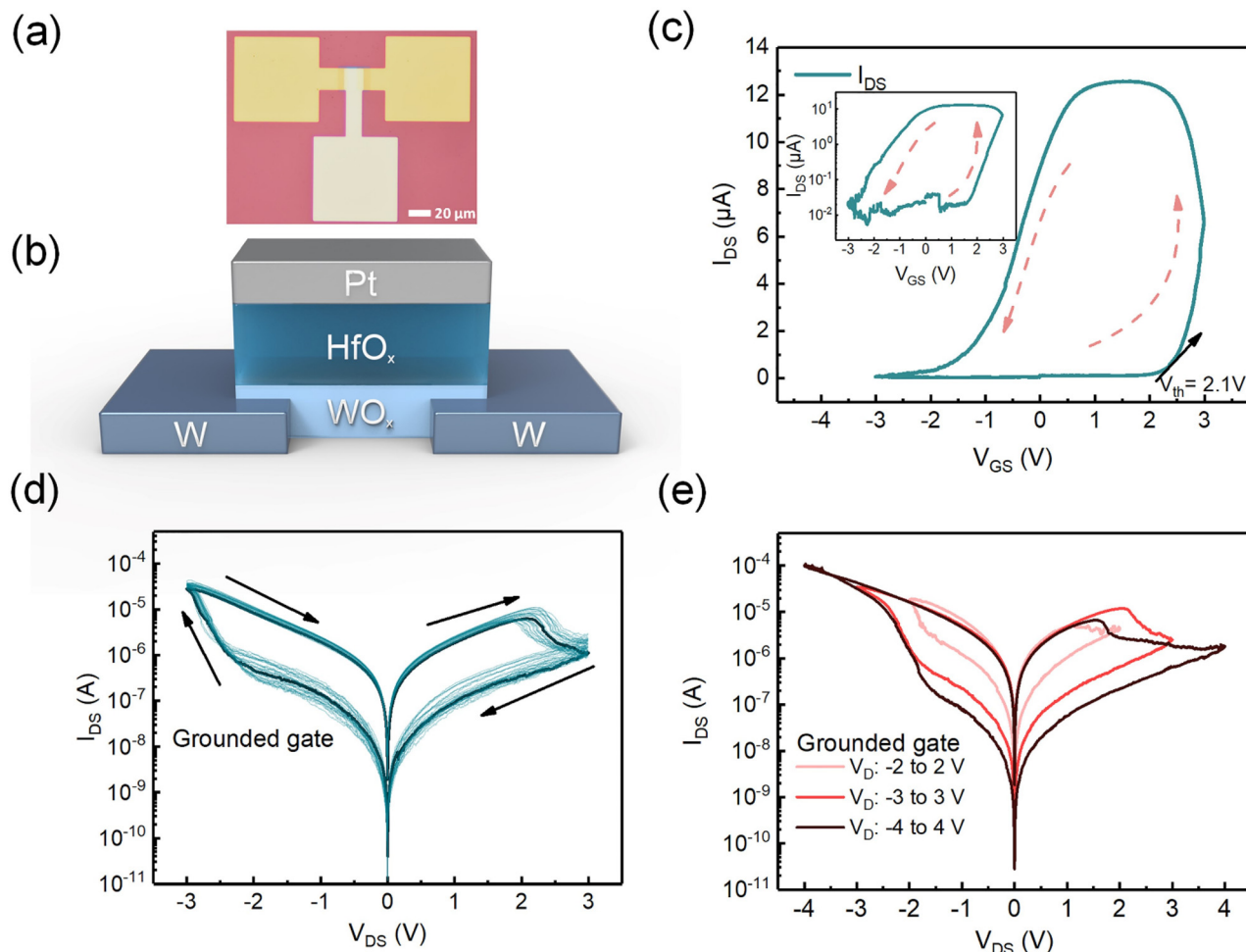


**Fig. 1** (a) Optical image and (b) schematic of the O-3TM structure. (c) Transfer characteristics of the O-3TM with the arrows indicating the sweeping direction. The inset gives the transfer curve on a log-linear scale. (d) 30 *I*-*V* cycles of the O-3TM with sweeping the drain voltage between -3 V and 3 V with  $V_g$  and  $V_s$  fixed at 0 V. The arrows indicate the directions of the current change. (e) *I*-*V* cycle of the device under -2 V, -3 to 3 V, and -4 to 4 V; a wider sweeping region has a more significant on/off ratio as more  $O^{2-}$  contributes to the current change.

threshold value (2.1 V). Then, the drop of the current is presented before the vanishing of  $V_{GS}$ , followed by the continuous decrease of  $I_{DS}$  under the negative  $V_{GS}$ .

The change of current is a result of the redox reaction occurring in the channel. Due to the oxygen-rich composition of the channel, the initial channel conductance of the pristine device is relatively low. Under an applied positive  $V_{GS}$ ,  $O^{2-}$  ions are extracted from the  $WO_x$  channel into the  $HfO_2$  electrolyte, leading to channel reduction and an increase in the  $I_{DS}$ . Conversely, the ions migrate oppositely under an applied negative  $V_{GS}$ , causing the channel to be oxidized again, resulting in a decrease in the  $I_{DS}$ . A threshold value of 2.1 V offers the minimum gate electric field for oxygen ion extraction. In addition, the  $I_{DS}$  drops before the  $V_{GS}$  becomes negative, revealing the volatility of the O-3TM. This shows that the extracted  $O^{2-}$  ions migrate back to the channel when the external electric field is insufficient to retain them in the electrolyte. The transfer characteristics under various  $V_{DS}$  are presented in Fig. S2a.† A greater  $V_{DS}$  provides a higher reading voltage for sensing the change in channel conductance, resulting in an elevated  $I_{DS}$  level. As the  $V_{DS}$  continues to rise, the effect of  $V_{GS}$  is compromised, leading to a lower effective gate electric field and a faster decline in the  $I_{DS}$ .

To further investigate the output characteristics of the O-3TM,  $V_{DS}$  was swept between  $-3$  and  $3$  V with  $V_{GS}$  fixed at  $0$  V. As shown in Fig. 1d, 30 cycles of  $I_{DS}$ - $V_{DS}$  curves were obtained in which the arrows indicate the current change direction. It shows a 'SET' and 'RESET' behavior similar to the RRAM device under negative and positive drain voltages, respectively.<sup>27–29</sup> Under a negative  $V_{DS}$ , the direction of the electric field at the channel/electrolyte interface points towards the channel, resulting in  $O^{2-}$  being extracted into the electrolyte, while the  $O^{2-}$  ions are driven to the channel when the applied  $V_{DS}$  is positive. It is important to note that there is an absence of delay between each cycle in Fig. 1d. When  $V_{DS}$  is only swept with negative polarity ( $0$  V to  $-3$  V to  $0$  V) and a delay is introduced between each cycle, the  $I_{DS}$ - $V_{DS}$  curves always originate from the low conductance state, as shown in Fig. S3.† When a short delay of  $200$  s is introduced, the channel conductance drifts to an intermediate state, and the initial conductance states for subsequent sweeps become progressively lower (Fig. S3a†). When a longer delay of  $1000$  s is applied, all  $O^{2-}$  ions migrate back to the channel, and a more stable low conductance state is observed (Fig. S3b†). The consistent  $I_{DS}$ - $V_{DS}$  curves in Fig. 1d indicate that the positive sweeping of  $V_{DS}$  yields similar results to the long delay, in which all  $O^{2-}$  ions are driven back to the channel by the applied electric field. This observation is in line with Fig. 1c, indicating the  $O^{2-}$  migration nature of the device. Furthermore, following the  $1000$  s delay, the positive sweeping of  $V_{DS}$  was conducted, as shown in Fig. S4.† In this case, the curve begins from a very low conductance state due to the self-migration of  $O^{2-}$  during the delay period, exhibiting a much smaller conductance window compared to its no-delay counterpart. The impact of  $V_{GS}$  on the output characteristics is also investigated. As shown in Fig. S2b,† a positive  $V_{GS}$  gives a

higher  $I_{DS}$  as it allows fewer  $O^{2-}$  ions to enter the channel. In contrast, a negative  $V_{GS}$  leads to a lower  $I_{DS}$  due to elevated  $O^{2-}$  ions within the channel. Thus, when  $V_{GS}$  equals  $-1$  V, the channel is enriched with  $O^{2-}$ , resulting in a notably narrower conductance window. Moreover, the  $V_{DS}$  was varied from  $\pm 2$  V to  $\pm 4$  V with a grounded gate, as presented in Fig. 1e. As the  $V_{DS}$  increases, a greater number of  $O^{2-}$  participate in the switching process, contributing to more pronounced hysteresis loops.

### Synaptic characteristics

In the biological brain, synaptic plasticity is used to describe the modulation of the synaptic weight, which determines the strength of the connection between neurons through potentiation or depression subject to the applied stimuli. Depending on the plasticity time course, synaptic plasticity can be generally divided into short-term plasticity (STP) and long-term plasticity (LTP).<sup>30–32</sup> The time course of a synapse can vary from milliseconds to an entire lifetime.<sup>33</sup> Synaptic plasticity presents an activity-dependent signature; in other words, weak stimuli induce STP, while strong stimuli induce LTP.

Consequently, STP-to-LTP transformation occurs when the duration and intensity of the stimuli are beyond a threshold.<sup>33</sup> For the developed O-3TM, the gate and source imitate the pre-synaptic and postsynaptic neurons, respectively, while the channel conductance representing the synaptic weight is read out by the drain terminal.<sup>34</sup> By applying pulse trains of different intensities, the ion extraction and relaxation would be affected, thus, demonstrating STP, LTP, and even the transition of STP to LTP.<sup>35,36</sup> Based on the gate-controlled ion extraction mechanism, when a presynaptic pulse is applied to the gate, the postsynaptic current  $I_{DS}$  exhibits a sudden increase, followed by a gradual decay back to its initial value once the pulse is removed, as revealed in Fig. 2a and c. Fig. 2a is obtained by varying the pulse amplitude while keeping the pulse width fixed at  $80$  ms, whereas Fig. 2c is obtained by varying the pulse width while keeping the pulse amplitude fixed at  $4$  V. Such a change in current triggered by an electrical spike is similar to the EPSC of a biological synapse.<sup>37</sup> The EPSC peak value grows exponentially as a function of both pulse amplitude and width, as illustrated in Fig. 2b and d. The rapid growth in the EPSC peak value corresponds to the movement of oxygen ions triggered by the presynaptic pulse. When the amplitude or width of the pulse is relatively small, insufficient ions are extracted, and a minimal current rise is expected. As the pulse width and amplitudes increase, the current increment becomes significantly more pronounced, exhibiting an exponential upward trend. Moreover, the relaxation time of  $I_{DS}$  to its initial state increases with the pulse width and amplitude, indicating the transition of the synaptic plasticity from short-term to long-term.<sup>38</sup> For neuromorphic computing applications, devices behaving with LTP are considered for memory/learning, while those showing STP are beneficial for critical computational functions in spatiotemporal information processing.<sup>39</sup>

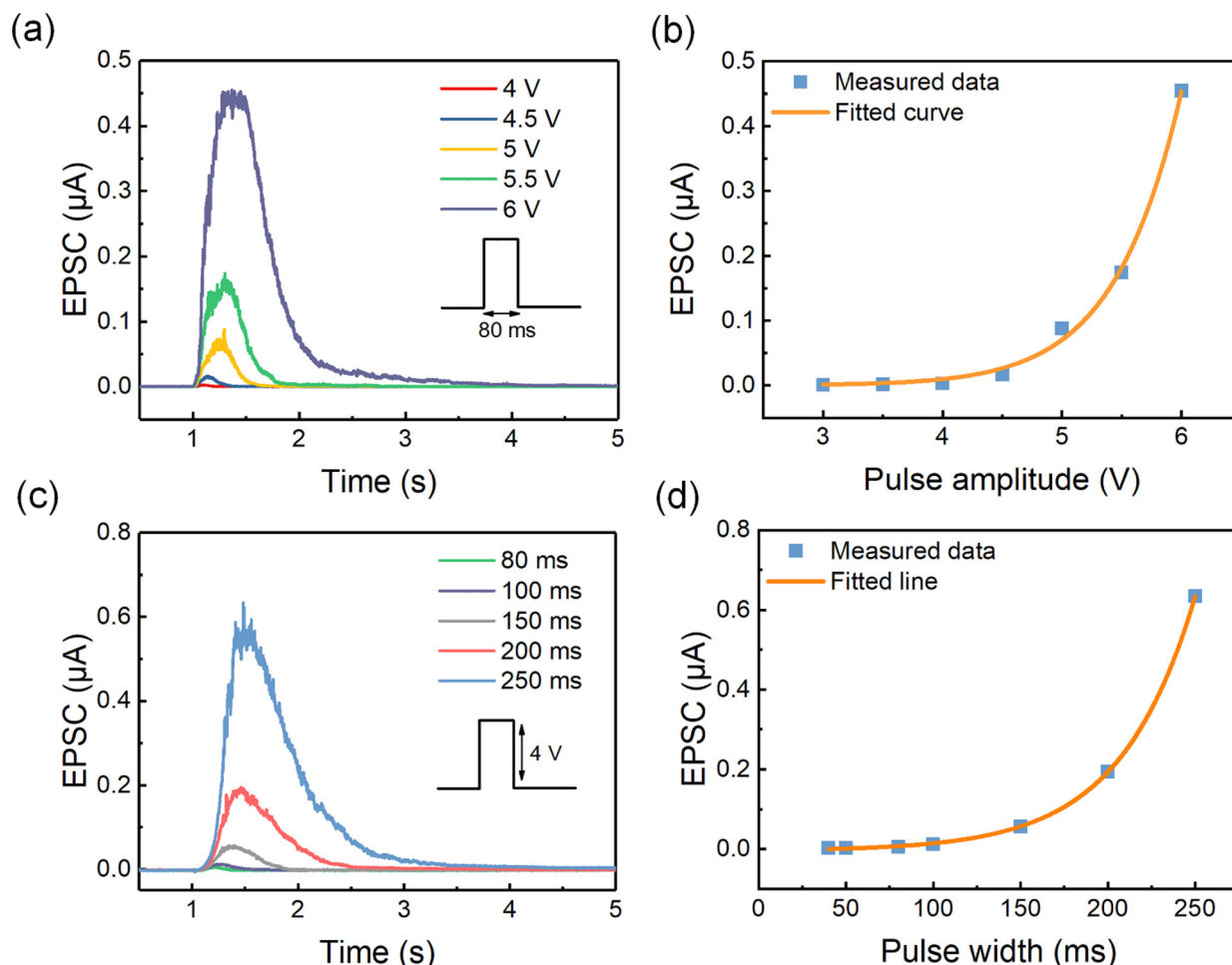


**Fig. 2** (a) EPSC under pulses with the same pulse width (80 ms) and varying amplitudes. (b) An exponential trend of the EPSC peak value versus the pulse amplitude. (c) EPSC under pulses with the same pulse amplitude (4 V) and varying widths. (d) The EPSC peak value increases exponentially with amplitude.

In addition to EPSC, the O-3TM device can also demonstrate PPF, *i.e.*, another form of STP, which is reported to be important for decoding temporal information in a biological system.<sup>34,40</sup> It is a phenomenon in neuroscience whereby the postsynaptic current caused by the second impulse is enhanced before the effect of the previous impulse is eliminated.<sup>41</sup> By applying two identical gate pulses consecutively, our device is capable of demonstrating a PPF effect, as presented in Fig. 3a. The EPSC triggered by the two gate pulses (5 V, 80 ms) with an interval of 100 ms and fixed  $V_{\text{DS}}$  as 0.2 V was obtained (unless otherwise specified,  $V_{\text{DS}}$  is always 0.2 V for all the following tests). The peak value of EPSC is enhanced by the second pulse ( $A_1 = 173$  nA,  $A_2 = 332$  nA). After the first pulse, the extracted  $\text{O}^{2-}$  ions do not have sufficient time to return to the channel entirely before the second pulse is delivered. Thus, the residual  $\text{O}^{2-}$  ions contribute to the total responding current. The PPF index is defined using the following equation:  $\text{PPF index} = (A_2/A_1) \times 100\%$ .<sup>39</sup> Fig. 3b gives the PPF index as a function of the pulse interval ( $\Delta t$ ). In the proposed device, a maximum PPF index of 229% was achieved

when  $\Delta t = 20$  ms, indicating a very strong temporal correlation at smaller intervals. As  $\Delta t$  rises, the facilitation efficiency drops. The data were fitted by a double phase exponential function:

$$\text{PPF index} = C_1 \times \exp(-\Delta t/\tau_1) + C_2 \times \exp(-\Delta t/\tau_2) + 1,$$

in which the  $C_1$  and  $C_2$  are initial facilitation magnitudes,  $\tau_1$  and  $\tau_2$  are the fitted time constants.<sup>42,43</sup> The decay process can be divided into two coupling phases: a rapid phase with a short relaxation time constant ( $\tau_1 = 33$  ms) and a subsequent slow phase with a large time constant ( $\tau_2 = 774$  ms),<sup>44–46</sup> which are commensurate in scale with that observed in biological synapses.<sup>47</sup>

We further demonstrate high-pass dynamics filtering using the STP properties of the device by applying multiple gate pulses with varying frequencies. As shown in Fig. 3c, 10 identical pulses (5 V, 20 ms) with varying frequencies were applied to the gate. To evaluate the filtering property, the amplitude gain is defined as  $|(A_{10} - A_1)/A_1|$ , where  $A_1$  and  $A_{10}$  are the EPSC peak values of the first and last pulses, respectively. As

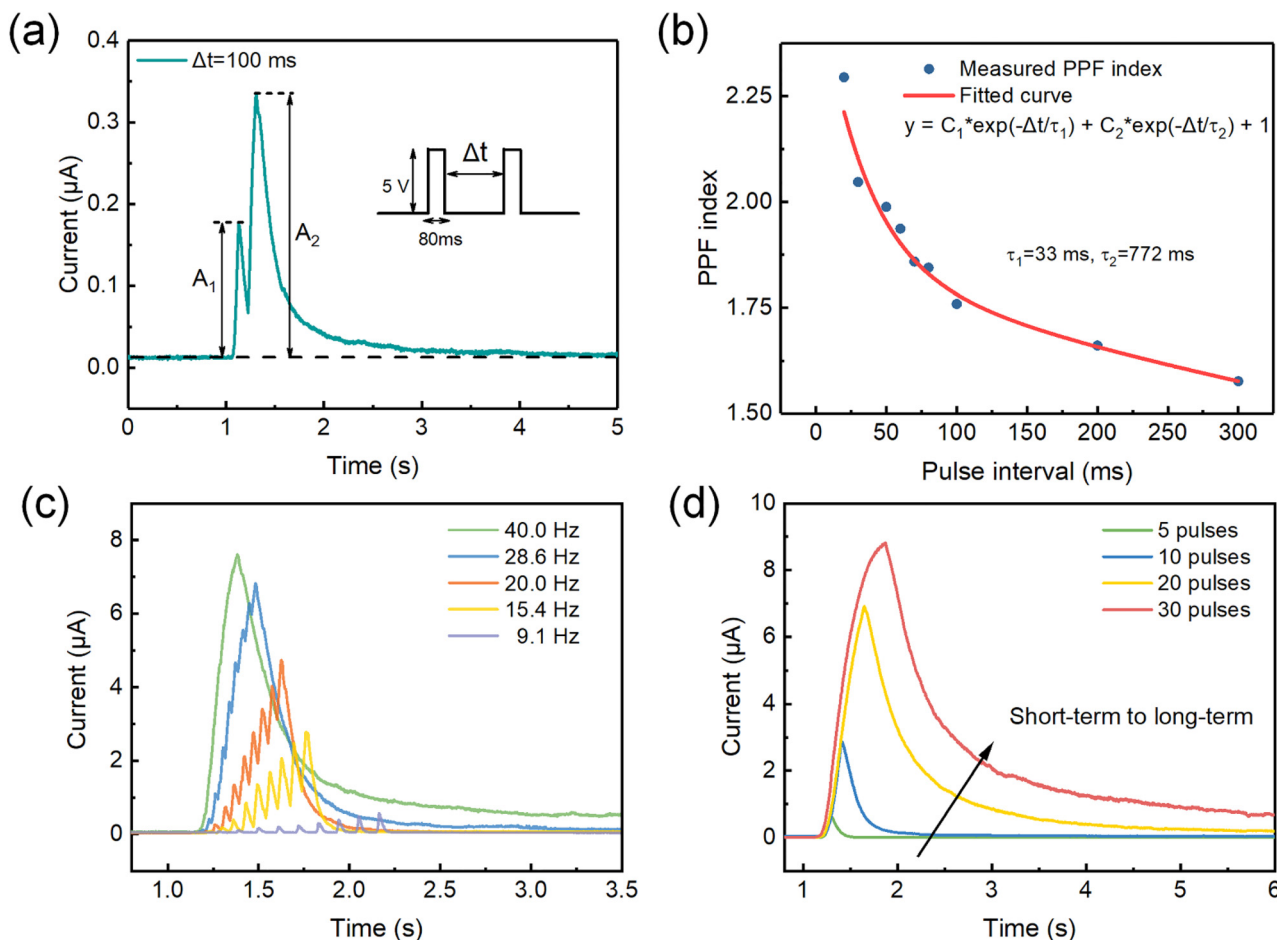


**Fig. 3** (a) PPF behavior achieved with two identical gate pulses (5 V, 80 ms) with a pulse interval of 100 ms. (b) PPF index plotted against the pulse interval, in which the solid line corresponds to the fitting curve of the double-phase exponential function. (c) EPSC obtained with 10 identical pulses (5 V, 20 ms) with different frequencies. (d) EPSC obtained with varying numbers of identical pulses (5 V, 20 ms, 40 Hz).

the stimulus frequency increases from 9.1 to 40 Hz, the amplitude gain rises from 35 to 505, suggesting a greater coupling between pulses with a higher stimulus frequency. This function is necessary for temporal computation in SNNs where the synapses would serve as dynamic filters when performing information transmission.<sup>6,33</sup> Additionally, another measurement was performed by applying different numbers of pulses with fixed frequencies (5 V, 20 ms, 40 Hz). As shown in Fig. 3d, the EPSC peak values exhibit a notable increase with more pulses, where more  $O^{2-}$  were extracted from the channel. The findings illustrated in Fig. 3c and d additionally suggest a correlation between an elevated EPSC peak value and a prolonged relaxation time, which aligns with the discussion presented in Fig. 2.

In this proposed bi-functional device, the key feature is the drifting of channel conductance due to  $O^{2-}$  diffusion. Thus, to investigate the uniformity and stability of the device, the same gate stimuli (30 pulses, 3 V, 50 ms) were applied to 10 devices, and the current decay was then monitored. As shown in Fig. S5,† the solid line indicates the average value of the current, and the error bars are the respective standard deviations. All devices show similar EPSC behaviours but with vari-

ations in the initial and maximum current levels, which can be attributed to the uniformity of the oxygen composition of the channels upon fabrication. Moreover, the same measurement was conducted 30 times in the same device for cycle-to-cycle variations (Fig. S6†), in which stable and repeatable switching is observed.

When a biological brain receives information, it will experience a learning process consisting of learning, forgetting, and relearning to perpetuate knowledge.<sup>44</sup> The relearning phase is influenced by the prior learning history, which can be more efficient compared to the first learning, as some neural pathways may still exist.<sup>48</sup> Here, our device successfully imitated the learning–forgetting–relearning process of a biological brain due to its  $O^{2-}$  diffusion properties (as shown in Fig. 4a). In the first learning process,  $n$  identical pulses (3 V, 50 ms) were applied to the gate, resulting in an increment in the channel current. Upon applying the  $n$  pulses, a reading voltage of 0.2 V was adopted to monitor the decaying current for 100 seconds. Finally, to emulate the relearning process,  $m$  pulses were applied to the gate until it reached the peak current in the first learning process. To ensure a consistent initial



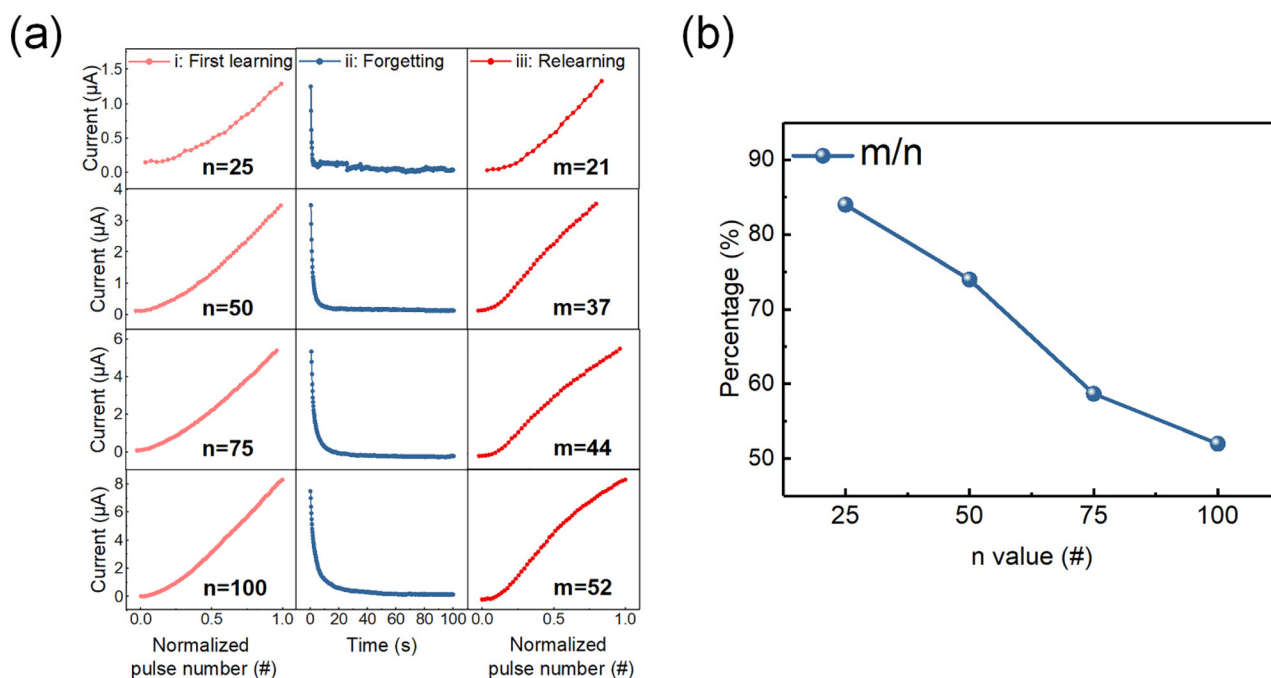


**Fig. 4** (a) The learning, forgetting, and relearning processes of the device with different numbers of pulses applied in the first learning process. (b) The ratio of pulse number in the relearning to the first learning process to achieve the same current level.

channel conductance, the device was allowed to relax, *i.e.*, zero external electric field, for a long period of time before each measurement. The results in Fig. 4a consistently show that  $m < n$  is valid across different values of  $n$ , indicating that fewer pulses are required in the relearning process. Moreover, as shown in Fig. 4b, when  $n$  increases, the ratio of  $m/n$  decreases. As such, we successfully demonstrate the learning–forgetting–relearning process in our devices.

### Neuronal characteristics

Apart from mimicking artificial synapses, the presented device also demonstrates neuronal functionality. Many models have been designed to mimic biological neurons, such as the integrate-and-fire (IF)<sup>49</sup> model, the leaky-integrate-and-fire (LIF)<sup>50</sup> model, and the Hodgkin–Huxley (H–H) model.<sup>51</sup> In an SNN, the LIF model is the most well-known model with the ability to demonstrate the three vital neuron functionalities, as its name suggests. Fig. 5a shows a schematic of the LIF model; the neuron is fired once its membrane potential reaches the threshold value. In recent years, artificial LIF neurons have been demonstrated in 2T Mott insulator-based memristors with threshold-switching properties or ion-diffusive devices.<sup>52–55</sup> Depending on the properties of the LIF neuronal devices, additional external control circuits are generally required, including a capacitor, a comparator, and a pulse generator.<sup>2,56–58</sup> As summarized in Table S1,<sup>†</sup> the reported memristor-based bi-functional devices generally require a capacitor for neuronal function emulation.

The volatility of the O-3TM arises from the current drifting caused by spontaneous  $\text{O}^{2-}$  diffusion. Therefore, unlike other

memristors such as SOI MOSFET, CMOS devices, and two-terminal Mott memristors, O-3TM has the ability to mimic an artificial LIF neuron without needing a capacitor.<sup>11,12,52–54</sup> Accordingly, the membrane potential is emulated by the channel current, while the input stimulus is represented by the applied gate pulses. Fig. 5b shows the repeatable LIF behavior achieved in the O-3TM with 10 integration pulses (3 V, 50 ms) and 1 firing pulse (–3 V, 50 ms), where a threshold of  $\sim 3.5 \mu\text{A}$  is observed. Schematics of  $\text{O}^{2-}$  migration under integrate, leaky and fire processes are displayed in Fig. 5c. For the integration function, the electric field (green arrow) induced by positive gate pulses extracts the  $\text{O}^{2-}$  and enhances the channel current. Under the opposite electric field (red arrow) introduced by a strong negative gate pulse,  $\text{O}^{2-}$  will be immediately driven back to the channel. The device is fired with the channel current dropping dramatically to the initial value.

The LIF behavior of the device is affected by many parameters, such as gate pulse amplitudes or widths and pulse intervals. To study the impact of these factors, pulses of different schemes were applied. Firstly, by varying the integration pulse (3 V) width from 20 ms to 60 ms, the achieved threshold current value increases from  $0.75 \mu\text{A}$  to  $9.7 \mu\text{A}$ , as presented in Fig. 6a. Additionally, the leakage time between each stimulus also determines the final threshold current value. Fig. 6b depicts the LIF behavior of the device under integration pulses (3 V, 50 ms) with pulse intervals varying from 20 ms to 60 ms. A shorter leakage time correlates to a higher threshold current, as fewer  $\text{O}^{2-}$  ions can diffuse back to the channel before the next stimulus. Fig. 6a and b suggest the

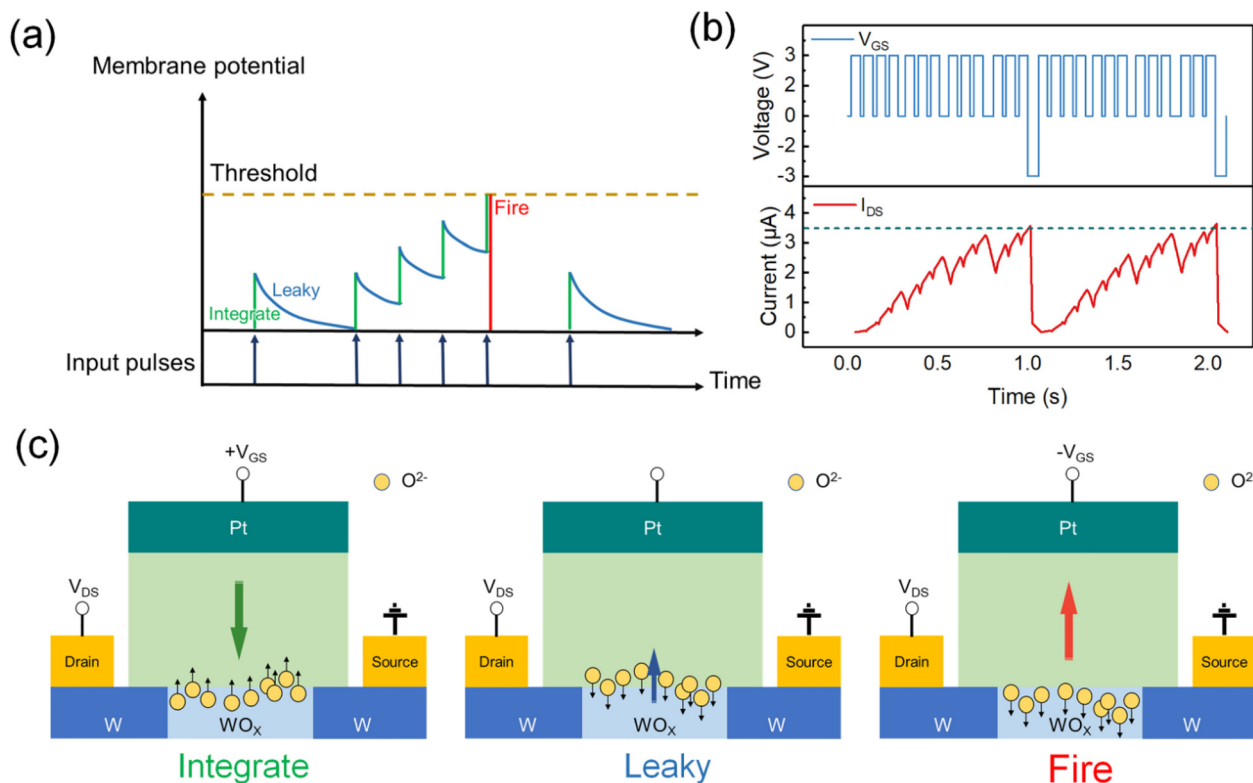


**Fig. 5** (a) Schematic of the LIF model. The neuron is fired once its membrane potential reaches the threshold value. (b) LIF behavior is emulated by the O-3TM, with the membrane potential represented by the current flow through the channel. Integration and firing pulses are 3 V, 50 ms and -3 V, 50 ms, respectively. (c)  $O^{2-}$  migration direction and the electric field direction (as the arrows indicate) under integrated, leaky and fire processes.

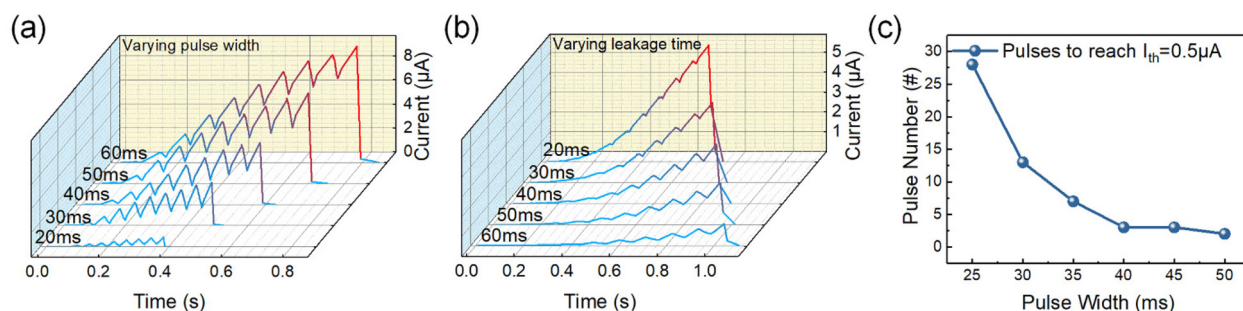


**Fig. 6** (a) LIF emulated by 10 pulses (3 V, leakage time 20 ms) with varying pulse widths. (b) LIF emulated by 10 pulses (3 V, 50 ms) with varying leakage times. (c) The required pulse number versus pulse width to reach the current threshold  $I_{th} = 0.5 \mu A$ .

tunability of the threshold value in the presented device, and a desired threshold value can be achieved by simply varying the pulse specification. For a threshold current of  $0.5 \mu A$ , only one pulse is required if its width is 50 ms, while 28 pulses are needed if the pulse width is reduced to 25 ms, as shown in Fig. 6c.

## Conclusions

In conclusion, a bi-functional O-3TM as a synapse and a neuron is developed. It can achieve synchronous program-

ming/reading and less random conductance modulation as a synapse than its 2T counterparts. The in- and out-flows of  $O^{2-}$  in the  $HfO_2$ -electrolyte and  $WO_x$ -channel tune the channel conductance, enabling it to mimic synaptic functions, including EPSC, PPF, high-pass filtering, and learning-forgetting-relearning. Furthermore, the LIF neuron functions are physically demonstrated by applying positive integration pulses and negative fire pulses. The leaky function is achieved through spontaneous  $O^{2-}$  diffusion upon the removal of gate stimuli, rather than by using external capacitors as in the reported works. Various desired thresholds can be obtained by simply adjusting the pulse scheme. With the capability of rea-

lizing both synaptic and neuronal functions, this work offers a more efficient and compatible method for enhancing current hardware neural network implementations.

## Methodology

The O-3TM was fabricated on a Si/SiO<sub>2</sub> substrate using a series of photolithography and magnetron sputtering steps. Before the device fabrication, the substrate was cleaned with acetone and isopropyl alcohol for 10 min each. First, 8 nm-thick W was deposited by DC sputtering as source/drain contact pads. Then, a 10 nm thick WO<sub>x</sub> was deposited as a channel using reactive oxygen sputtering using a W target. The flow rates of O<sub>2</sub> and Ar gases were fixed at 15 and 5 sccm during the sputtering process. Subsequently, 30 nm HfO<sub>2</sub> electrolyte and 15 nm Pt top electrodes were deposited by RF and DC sputtering, respectively. The dimension of the device channel is 20 × 10 μm (width × length), which is defined by the distance between the patterned source and drain pads. All sputtering processes were maintained at 2 mTorr and room temperature using an AJA International ATC-Orion 8 target UHV magnetron sputter deposition system with a power of 50 W. Electrical characterization of the device was performed with a Keithley 4200A SCS parameter analyzer in an ambient environment at room temperature. XPS data were obtained using a Kratos Analytical, AXIS Supra system.

## Author contributions

L. L. conceived the research and wrote the manuscript. P. A. D. and C. C. I. A. designed and participated in the experiments. E. K. K., G. J. L., H. Y. P., M. Y. C., and C. X. X. L. analysed the results. W. S. L. supervised and sponsored the research. All authors reviewed and revised the manuscript.

## Conflicts of interest

There are no conflicts to declare.

## Acknowledgements

This work was supported by a RIE2020 ASTAR AME IAF-ICP Grant (No. I1801E0030).

## References

- 1 D. Kim, Y. R. Jeon, B. Ku, C. Chung, T. H. Kim, S. Yang, U. Won, T. Jeong and C. Choi, *ACS Appl. Mater. Interfaces*, 2021, **13**, 52743–52753.
- 2 J. Q. Yang, R. Wang, Z. P. Wang, Q. Y. Ma, J. Y. Mao, Y. Ren, X. Yang, Y. Zhou and S. T. Han, *Nano Energy*, 2020, **74**, 104828.
- 3 G. Pedretti and D. Ielmini, *Electronics*, 2021, **10**, 1063.
- 4 J. Lu, Y. Li, Z. Xuan, H. Xu, S. Wu, Z. Wang, S. Long, Q. Liu and D. Shang, *IEEE Electron Device Lett.*, 2022, **43**, 296–299.
- 5 W. H. Brigner, J. S. Friedman, N. Hassan, L. Jiang-Wei, X. Hu, D. Saha, C. H. Bennett, M. J. Marinella, J. A. C. Incorvia and F. Garcia-Sanchez, *IEEE Trans. Electron Devices*, 2019, **66**, 4970–4975.
- 6 Q. Wan, M. Rasetto, M. T. Sharbati, J. R. Erickson, S. R. Velagala, M. T. Reilly, Y. Li, R. Benosman and F. Xiong, *Adv. Intell. Syst.*, 2021, **3**, 2100021.
- 7 J. Li, Y. Yang, M. Yin, X. Sun, L. Li and R. Huang, *Mater. Horiz.*, 2020, **7**, 71–81.
- 8 Y. Cao, T. Zhao, C. Zhao, Y. Liu, P. Song, H. Gao and C. Z. Zhao, *J. Mater. Chem. C*, 2022, **10**, 3196–3206.
- 9 Y. Fu, Y. Zhou, X. Huang, B. Dong, F. Zhuge, Y. Li, Y. He, Y. Chai and X. Miao, *Adv. Funct. Mater.*, 2022, **32**, 2111996.
- 10 J.-K. Han, J. Oh, G.-J. Yun, D. Yoo, M.-S. Kim, J.-M. Yu, S.-Y. Choi and Y.-K. Choi, *Sci. Adv.*, 2021, **7**, eabg8836.
- 11 J.-K. Han, M. Seo, W.-K. Kim, M.-S. Kim, S.-Y. Kim, M.-S. Kim, G.-J. Yun, G.-B. Lee, J.-M. Yu and Y.-K. Choi, *IEEE Electron Device Lett.*, 2020, **41**, 208.
- 12 S. Dutta, V. Kumar, A. Shukla, N. R. Mohapatra and U. Ganguly, *Sci. Rep.*, 2017, **7**, 8257.
- 13 J. Zhao, Y. Ran, Y. Pei, Y. Wei, J. Sun, Z. Zhang, J. Wang, Z. Zhou, Z. Wang, Y. Sun and X. Yan, *Mater. Horiz.*, 2023, **10**, 4521–4531.
- 14 S. H. Sung, T. J. Kim, H. Shin, T. H. Im and K. J. Lee, *Nat. Commun.*, 2022, **13**, 2811.
- 15 J. Woo, D. Lee, Y. Koo and H. Hwang, *Microelectron. Eng.*, 2017, **182**, 42.
- 16 J. Woo, K. Moon, J. Song, S. Lee, M. Kwak, J. Park and H. Hwang, *IEEE Electron Device Lett.*, 2016, **37**, 994.
- 17 X. Ji, C. Wang, K. G. Lim, C. C. Tan, T. C. Chong and R. Zhao, *ACS Appl. Mater. Interfaces*, 2019, **11**, 20965–20972.
- 18 J. Cui, F. An, J. Qian, Y. Wu, L. L. Sloan, S. Pidaparthi, J. M. Zuo and Q. Cao, *Nat. Electron.*, 2023, **6**, 292–300.
- 19 X. Zhang, S. Wu, R. Yu, E. Li, D. Liu, C. Gao, Y. Hu, T. Guo and H. Chen, *Matter*, 2022, **5**, 3023–3040.
- 20 A. Sebastian, R. Pendurthi, A. Kozhakhmetov, N. Trainor, J. A. Robinson, J. M. Redwing and S. Das, *Nat. Commun.*, 2022, **13**, 6139.
- 21 R. D. Nikam, M. Kwak and H. Hwang, *Adv. Electron. Mater.*, 2021, **7**, 2100142.
- 22 J. Lee, R. D. Nikam, M. Kwak and H. Hwang, *IEEE Trans. Electron Devices*, 2022, **69**, 2218–2221.
- 23 J. Lee, R. D. Nikam, M. Kwak, H. Kwak, S. Kim and H. Hwang, *Adv. Electron. Mater.*, 2021, **7**, 2100219.
- 24 C. Lee, K. G. Rajput, W. Choi, M. Kwak, R. D. Nikam, S. Kim and H. Hwang, *IEEE Electron Device Lett.*, 2020, **41**, 1500.
- 25 L. Liu, P. A. Dananjaya, M. Y. Chee, G. J. Lim, C. X. X. Lee and W. S. Lew, *ACS Appl. Mater. Interfaces*, 2023, **15**, 29287–29296.



- 26 J. Lee, R. D. Nikam, S. Lim, M. Kwak and H. Hwang, *Nanotechnology*, 2020, **31**, 235203.
- 27 P. A. Dananjaya, D. J. J. Loy, S. C. W. Chow and W. S. Lew, *ACS Appl. Electron. Mater.*, 2019, **1**, 2076–2085.
- 28 K. Hou, S. Chen, C. Zhou, L. L. Nguyen, P. A. Dananjaya, M. Duchamp, G. C. Bazan, W. S. Lew and W. L. Leong, *Nano Lett.*, 2021, **21**, 9262–9269.
- 29 M. Y. Chee, P. A. Dananjaya, G. J. Lim, Y. Du and W. S. Lew, *ACS Appl. Mater. Interfaces*, 2022, **14**, 35959–35968.
- 30 L. Zhang, Z. Tang, J. Fang, X. Jiang, Y. Jiang and Q. Sun, *Appl. Surf. Sci.*, 2022, **606**, 154718.
- 31 H. Han, H. Yu, H. Wei, J. Gong and W. Xu, *Small*, 2019, **15**, 1900695.
- 32 H. Li, T. Liu, Y. Wang, S. Geng, T. Xu, M. Cao, S. Fan, T. Liu and J. Su, *Ceram. Int.*, 2022, **48**, 13754–13760.
- 33 R. Yang, H. M. Huang and X. Guo, *Adv. Electron. Mater.*, 2019, **5**, 1900287.
- 34 G. Gou, J. Sun, C. Qian, Y. He, L. A. Kong, Y. Fu, G. Dai, J. Yang and Y. Gao, *J. Mater. Chem. C*, 2016, **4**, 11110.
- 35 Q. Liu, L. Yin, C. Zhao, Z. Wu, J. Wang, X. Yu, Z. Wang, W. Wei, Y. Liu, I. Z. Mitrovic, L. Yang, E. G. Lim and C. Z. Zhao, *Nano Energy*, 2022, **97**, 107171.
- 36 X. Wang, L. Zhu, C. Chen, H. Mao, Y. Zhu, Y. Zhu, Y. Yang, C. Wan and Q. Wan, *Flexible Printed Electron.*, 2021, **6**, 04400.
- 37 C. Han, X. Han, J. Han, M. He, S. Peng, C. Zhang, X. Liu, J. Gou and J. Wang, *Adv. Funct. Mater.*, 2022, **32**, 2113053.
- 38 R. Yu, E. Li, X. Wu, Y. Yan, W. He, L. He, J. Chen, H. Chen and T. Guo, *ACS Appl. Mater. Interfaces*, 2020, **12**, 15446–15455.
- 39 G. Lee, J. H. Baek, F. Ren, S. J. Pearton, G. H. Lee and J. Kim, *Small*, 2021, **17**, 2100640.
- 40 C.-S. Yang, D.-S. Shang, N. Liu, E. J. Fuller, S. Agrawal, A. A. Talin, Y.-Q. Li, B.-G. Shen and Y. Sun, *Adv. Funct. Mater.*, 2018, **28**, 1804170.
- 41 P. Feng, W. Xu, Y. Yang, X. Wan, Y. Shi, Q. Wan, J. Zhao and Z. Cui, *Adv. Funct. Mater.*, 2017, **27**, 1604447.
- 42 S. H. Kim and W. J. Cho, *Int. J. Mol. Sci.*, 2021, **22**, 1344.
- 43 J. Park, C. Oh and J. Son, *J. Mater. Chem. C*, 2021, **9**, 2521–2529.
- 44 W. C. Yang, Y. C. Lin, S. Inagaki, H. Shimizu, E. Ercan, L. C. Hsu, C. C. Chueh, T. Higashihara and W. C. Chen, *Adv. Sci.*, 2022, **9**, 2105190.
- 45 X. Li, B. Yu, B. Wang, L. Bao, B. Zhang, H. Li, Z. Yu, T. Zhang, Y. Yang, R. Huang, Y. Wu and M. Li, *Nanoscale*, 2020, **12**, 16348–16358.
- 46 S. E. Ng, J. Yang, R. A. John and N. Mathews, *Adv. Funct. Mater.*, 2021, **31**, 2100807.
- 47 J. Chen, J. Xu, J. Chen, L. Gao, C. Yang, T. Guo, Y. Zhao, Y. Xiao, J. Wang and Y. Li, *Mater. Today Commun.*, 2022, **32**, 103957.
- 48 M. L. Schlichtinga and A. R. Prestona, *Proc. Natl. Acad. Sci. U. S. A.*, 2014, **111**, 15845–15850.
- 49 D. Lee, M. Kwak, K. Moon, W. Choi, J. Park, J. Yoo, J. Song, S. Lim, C. Sung, W. Banerjee and H. Hwang, *Adv. Electron. Mater.*, 2019, **5**, 1800866.
- 50 Z. Wang, S. Joshi, S. Savel'Ev, W. Song, R. Midya, Y. Li, M. Rao, P. Yan, S. Asapu, Y. Zhuo, H. Jiang, P. Lin, C. Li, J. H. Yoon, N. K. Upadhyay, J. Zhang, M. Hu, J. P. Strachan, M. Barnell, Q. Wu, H. Wu, R. S. Williams, Q. Xia and J. J. Yang, *Nat. Electron.*, 2018, **1**, 137–145.
- 51 H. M. Huang, R. Yang, Z. H. Tan, H. K. He, W. Zhou, J. Xiong and X. Guo, *Adv. Mater.*, 2019, **31**, 1803849.
- 52 C. Adda, B. Corraze, P. Stoliar, P. Diener, J. Tranchant, A. Filatre-Furcate, M. Fourmigué, D. Lorcy, M. P. Besland, E. Janod and L. Cario, *J. Appl. Phys.*, 2018, **124**, 152124.
- 53 P. Stoliar, J. Tranchant, B. Corraze, E. Janod, M. P. Besland, F. Tesler, M. Rozenberg and L. Cario, *Adv. Funct. Mater.*, 2017, **27**, 1604740.
- 54 Y. Fu, Y. Zhou, X. Huang, B. Dong, F. Zhuge, Y. Li, Y. He, Y. Chai and X. Miao, *Adv. Funct. Mater.*, 2022, **32**, 2111996.
- 55 S. Hao, X. Ji, S. Zhong, K. Y. Pang, K. G. Lim, T. C. Chong and R. Zhao, *Adv. Electron. Mater.*, 2020, **6**, 1901335.
- 56 N. M. Samardzic, J. S. Bajic, D. L. Sekulic and S. Dautovic, *Electronics*, 2022, **11**, 894.
- 57 Z. Wu, J. Lu, T. Shi, X. Zhao, X. Zhang, Y. Yang, F. Wu, Y. Li, Q. Liu and M. Liu, *Adv. Mater.*, 2020, **32**, 2004398.
- 58 H.-M. Huang, Z. Wang, T. Wang, Y. Xiao and X. Guo, *Adv. Intell. Syst.*, 2020, **2**, 2000149.